Transition boiling bubble powered micro-engine using a Leidenfrost bearing

Transition boiling bubble powered micro-engine using a Leidenfrost bearing

Prashant Agrawal[1*], Anthony Buchoux[2], Gary G. Wells[1,2], Rodrigo Ledesma-Aguilar[1,2], Anthony J. Walton[2], Jonathan G. Terry[2], Glen McHale[1,2], Khellil Sefiane[2], and Adam A. Stokes[2*]

[1]Smart Materials and Surfaces Laboratory, Faculty of Engineering & Environment, Northumbria University, Newcastle upon Tyne, UK
[2]School of Engineering, The University of Edinburgh, Edinburgh, UK
[*]Corresponding authors: prashant.agrawal@northumbria.ac.uk & adam.stokes@ed.ac.uk

Abstract

Overcoming friction while generating useful torque is a challenge for micro engines. Here we report the development of a microscale engine that utilizes transition boiling as a mode of propulsion and the Leidenfrost effect as a friction-less bearing. The transition boiling micro engine shows significantly improved performance compared to a Leidenfrost engine, which uses vapor entrainment as a propulsion mechanism (up to 3 orders of magnitude higher efficiency). We characterise the performance of the transition boiling engine with temperature and develop an analytical model to model and compare the engine performance with experimental observations. Our results provide a new approach to generating torque with a virtually frictionless bearing in micro-engines unlocking applications in, e.g., remote sensing and low-grade energy harvesting.

Keywords: Leidenfrost, transition boiling, vapor bearing, heat engine, thin-film boiling

1 Introduction

Thermal energy harvesting at microscales is promising for applications in remote sensing, space exploration and low grade energy harvesting [1, 2]. Advancements in micromachining and 3D printing have provided opportunities to scale down macro-scale gas and vapor cycle-based rotary and reciprocatory thermo-mechanical engines [3, 4]. A low inertia favours the development of such millimetric and micro-scale engines, but an increased surface area to volume ratio increases energy losses and component wear due to solid friction [5, 6]. However, new mechanisms that exploit this increased surface area to volume ratio have been explored to induce motion such as using drop impact [7] and micro-bubbles [8, 9]. Friction on moving components at these small scales can be overcome by removing direct contact between a stator and a rotor via levitation using electrostatic [10] and magnetic [11] fields or through gas or liquid hydrodynamic bearings [12, 13]. Primarily developed for driving micromotors, the application of these technologies is limited as they involve multi-component design and complex machining processes.

Recently, the Leidenfrost effect has been exploited to provide simultaneous self-propulsion and hydrodynamic lubrication, working as a virtually frictionless heat engine [14–16]. Here, a liquid drop levitates on a cushion of its own vapor on a superheated substrate [17], and undergoes self-propulsion in the presence of asymmetric substrate textures [18–24] or asymmetries in the levitating mass [25–27]. Such a self propulsion can also be obtained at temperatures lower than the Leidenfrost temperature on superhydrophobic surfaces due to reduced heat transfer [28–30]. Although this mechanism provides a simplified operational design for in-situ lubrication and

energy conversion, the viscous drag driven propulsion [31] results in low propulsion torque and power outputs.

In this work, a heat engine is presented where the virtually frictionless properties of Leidenfrost levitation is integrated with the dynamics of transition boiling. The short time scale dynamics of bubble growth has been widely used in inkjet printing [32, 33] and, more recently, for micro-propulsion in micro-thrusters [34, 35] and micro-motors [36, 37]. This work employs these millisecond time dynamics of bubble nucleation to rapidly propel a solid coupled to a liquid rotor in a Leidenfrost state on a heated substrate. These two states are simultaneously achieved by radially positioning bubble nucleation sites, via machined rough features, on a smooth substrate. A simple analytical model is proposed to understand the dynamics of this engine and compare the rotation outputs with a Leidenfrost engine [14] of the same system size. By eliminating solid friction, this millimetric scale bubble powered engine is able to generate power outputs of the order of 10 µW, significantly higher than previously developed bubble powered devices [38, 39]. Apart from converting heat to mechanical energy, such controlled bubble-powered propulsion devices can also be used for mixing bio-reagents in lab-on-a-chip devices [40] and electronic coolants in microgravity conditions [41].

2 Experimental setup

Figure 1 (a) and (b) show a schematic and an experimental view of the transition boiling engine. A key component of the engine is the thin-sheet containing three indents (1 mm x 0.3 mm x 0.2 mm), positioned radially at the centre of the engine (Figure 1 (c) and (d)), to create localised bubble nucleation sites. The indents are angled away from the substrate as shown in Fig. 1 (e) and (f). This thin sheet is sandwiched between the heated substrate and a confinement well (Figure 1 (a)). The smooth surface of the confinement well contains the liquid drop, coupled to an aluminium rotor (diameter d_p =7 mm and thickness h_p =1 mm) via surface tension, and ensures the liquid is in a Leidenfrost state with the walls of the well. A black line is marked on the rotor for tracking its rotation speed.

The setup is placed on hotplate (Stuart UC-150) and the temperature at the base of the well is recorded via a thermocouple placed by the side of the engine (Figure 1 (b)). A fixed volume of water is inserted in the well and the aluminium rotor is lowered on the drop within 5 seconds of depositing the water. The temperature is recorded before injecting the liquid, during the operation of the engine and after the rotation has stopped. The temperatures reported in this study are an average of these three temperatures, which provides a maximum standard deviation of ±5 °C. The rotation of the rotor is recorded at 500 fps (IDS UI-3130CP) for a maximum recording time of 15 seconds.

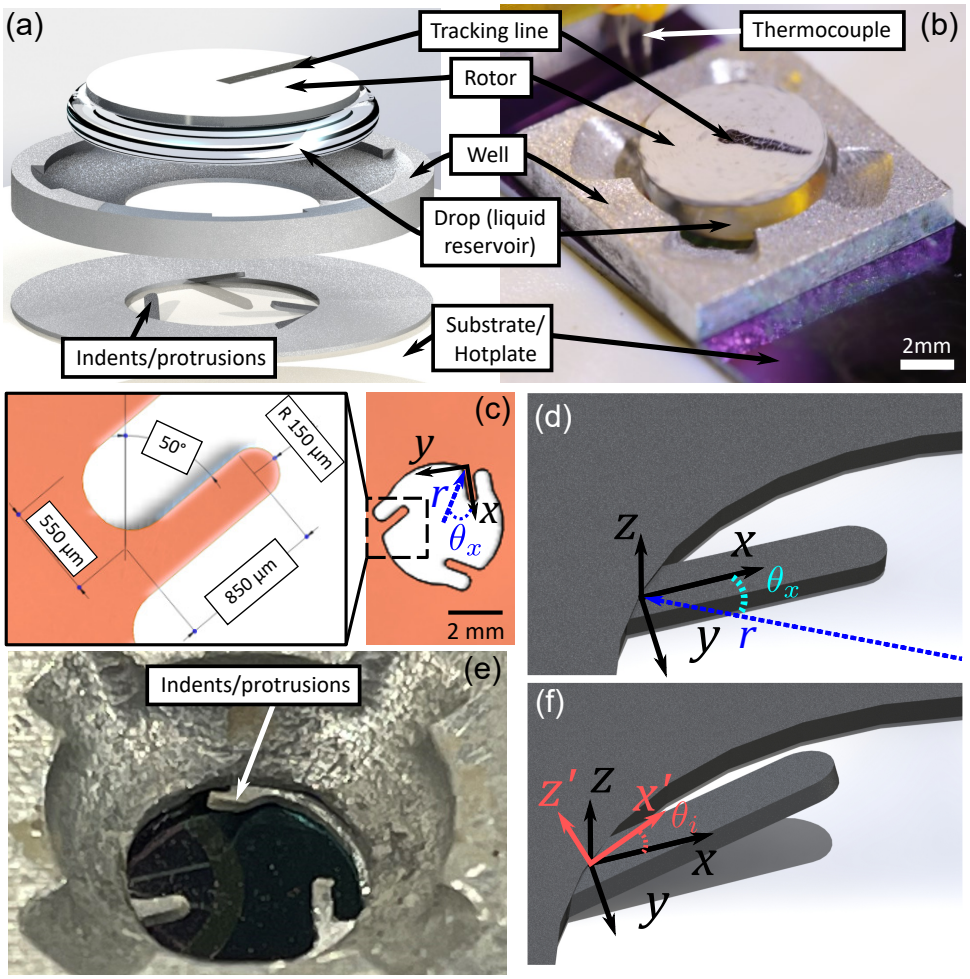

Figure 1: (a) 3D render of the different components of a transition boiling engine; (b) Experimental view of the engine with the liquid and the solid rotor; (c) Schematic view of the indent dimensions after planar fabrication; θ_x is the angle between the x-axis and the r-axis; (d) 3D render of the planar fabricated indents indicating the angle θ_x; (e) Experimental view of the indents after bending away from the substrate (about the y-axis); (f) 3D render of the indents bent away from the substrate after rotation by θ_i about the y-axis.

3 Results

Figure 2 shows a typical rotation sequence of the solid-liquid rotor, starting from rest. During its operation, the water remains in the Leidenfrost state over the heated substrate but undergoes transition boiling on the indents. The rotation is driven by the bubbles generated from these nucleation sites, identified by an audible bubbling sound during operation. If the bubbling sound is absent, the rotor either does not rotate or rotates randomly, which indicates a Leidenfrost state on the indents; this random rotation is because of internal flows generated in a random directions in a Leidenfrost drops [25]. The rotation direction is opposite to the orientation of the indents, i.e, the rotor rotates in the clockwise direction for counter-clockwise pointing indents (as in Figure 2 (a)) and vice-versa (Figure 2 and Supplementary video SV1).

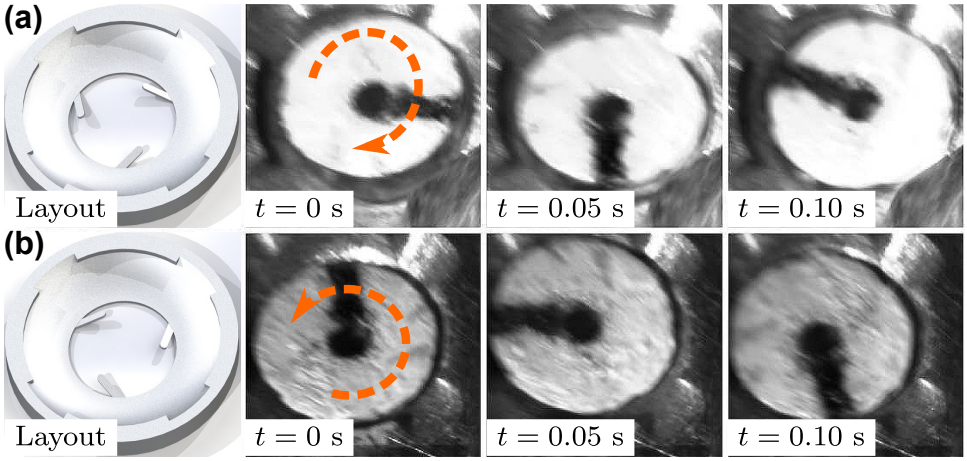

Figure 2: Controlling rotation direction of rotor in a transition boiling engine: (a) Counter-clockwise pointing indents; (b) Clockwise pointing indents. For both experiments $V_d = 50\,\mu L$ and T_w =285 °C. Supplementary video SV1.

Figure 3 shows typical evolution of the angular speed of the rotor (ω) over time for different liquid volumes (V_d) and substrate temperatures (T_w). The rotor accelerates from rest and rotates at a constant terminal angular speed (ω_t) till either the solid rotor collides with the well or the liquid is exhausted. The rotation can be sustained by replenishing the liquid, as can be observed in Fig. 3, represented by green circles (V_d =50 µL, T_w =245 °C) and Supplementary video SV3. The terminal rotation speeds are strongly dependent on the deposited volume (Figure 4 (a)). A larger deposited droplet volume equates to lower terminal speed (comparing the 50 µL and 100 µL), however the 140 µL droplet demonstrates a larger speed than the 100 µL. This is likely because the drop is large enough to interact with the top of the side walls of the well where there are bubbles being formed and creating stronger flows inside. There are only two temperatures reported for these experiments with V_d=140 µL as at lower temperatures there was vigorous boiling and no stable rotation could be observed, while at higher temperatures, the liquid is in a Leidenfrost state with the side walls completely, therefore no additional bubbles from the top of the side walls was observed. Additionally, it also likely that the flows generated from the bubbles on the indents dissipate in this larger liquid volume before reaching the solid rotor, therefore, no consistent rotation was observed. By restricting the height of the liquid volume, either naturally to twice the capillary length [19] by altering the geometry of the side walls or by manually controlling the position of the solid rotor [16], the operating temperature range of the engine can be increased at higher drop volumes.

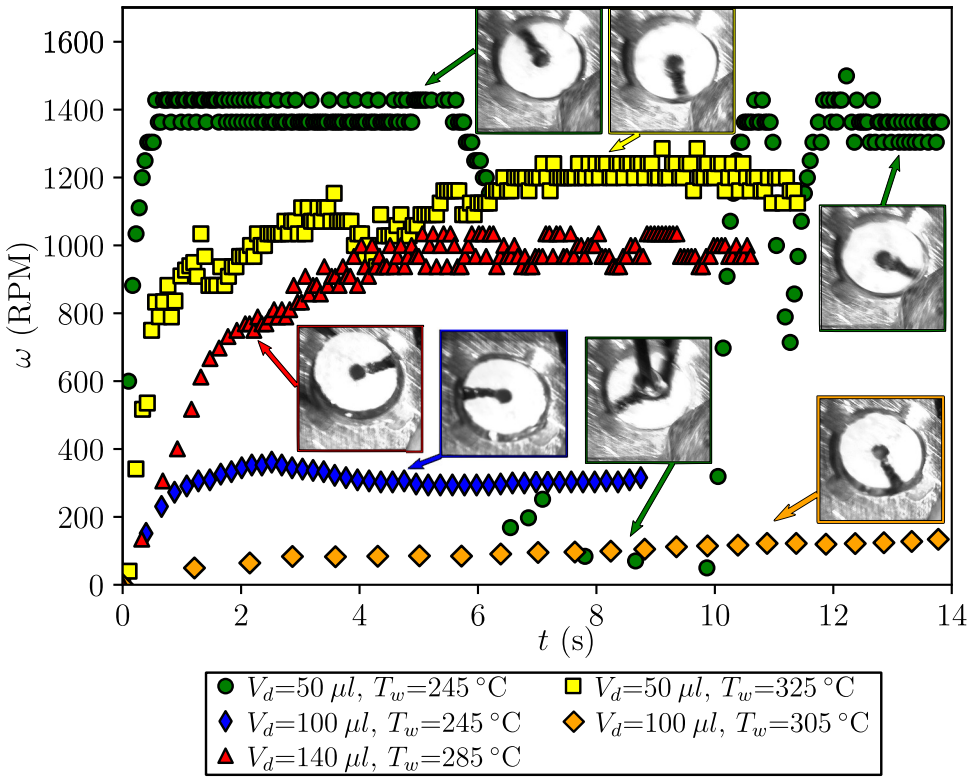

Figure 3: Typical evolution of rotation speeds at different deposited volumes of the liquid (V_d) and substrate temperatures (T_w). Supplementary video SV2.

Due to the nature of propulsion, the engine operates in a narrow temperature range. The minimum operating temperature limit is determined by the Leidenfrost temperature on the walls and the substrate to allow reduced friction due to levitation. For example, in the present experiments with Aluminum as the substrate and water as the liquid, the Leidenfrost temperature is around 225 °C. By lowering the Leidenfrost temperature, either by using a highly volatile liquid [42, 43], low pressure environment [44] or superhydrophobic coatings [28], this minimum operating temperature can be lowered.

The maximum operating temperature limit is determined by the Leidenfrost temperature on the indents and their geometry, which indicates a termination of bubble nucleation driving the rotation. To increase the maximum operating temperature, the indents can be selectively roughened to increase the Leidenfrost temperature relative to the substrate and the walls. The indents should also penetrate the liquid volume to induce bubble nucleation. Therefore, their shape and length would also affect the onset of the Leidenfrost state.

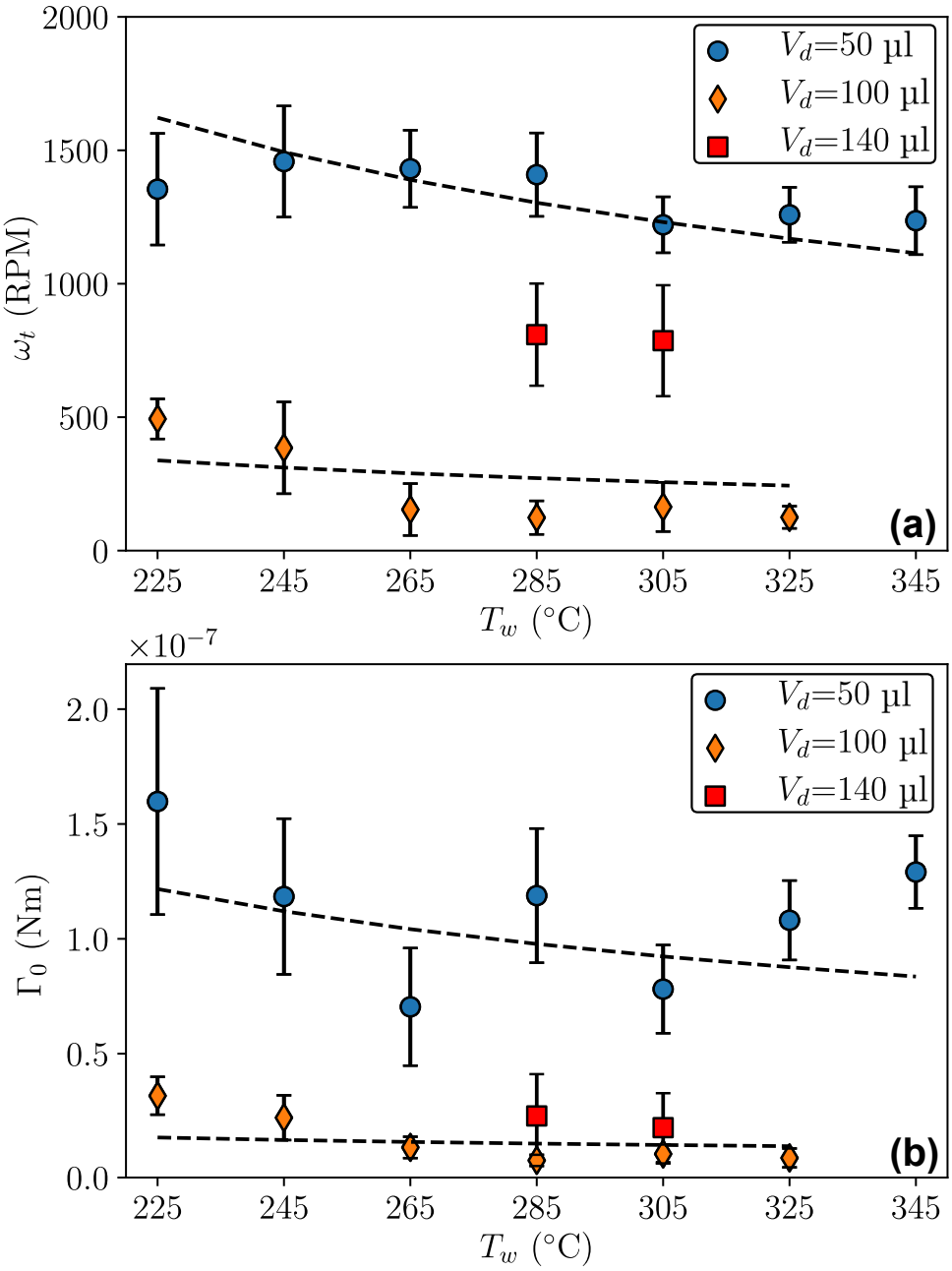

Figure 4: Variation of (a) Terminal angular speed (ω_t) and (b) Initial torque (Γ_0) with substrate temperature (T_w). Dashed lines are fit curves corresponding to $q'' \propto \Delta T^{-1.28}$ [45], derived via equation 1 and 7.

4 Discussion

The underlying mechanism driving the rotation can be attributed to the evaporation momentum force [46]. When a liquid undergoes phase change at the liquid-vapor interface (Figure 5 (a)), the velocity of the vapor is higher than that of the liquid (proportional to the ratio of density of the liquid to that of the vapor). This sudden ejection of vapor from the interface produces a reaction force which pulls the interface into the liquid, i.e. the bubble expands. For a 2D geometry, the evaporative momentum force (F_M) can be written as [46, 47]:

$$F_M = \frac{q_I''^{\,2}}{h_{lv}} \frac{A_{sf}}{\rho_v}. \tag{1}$$

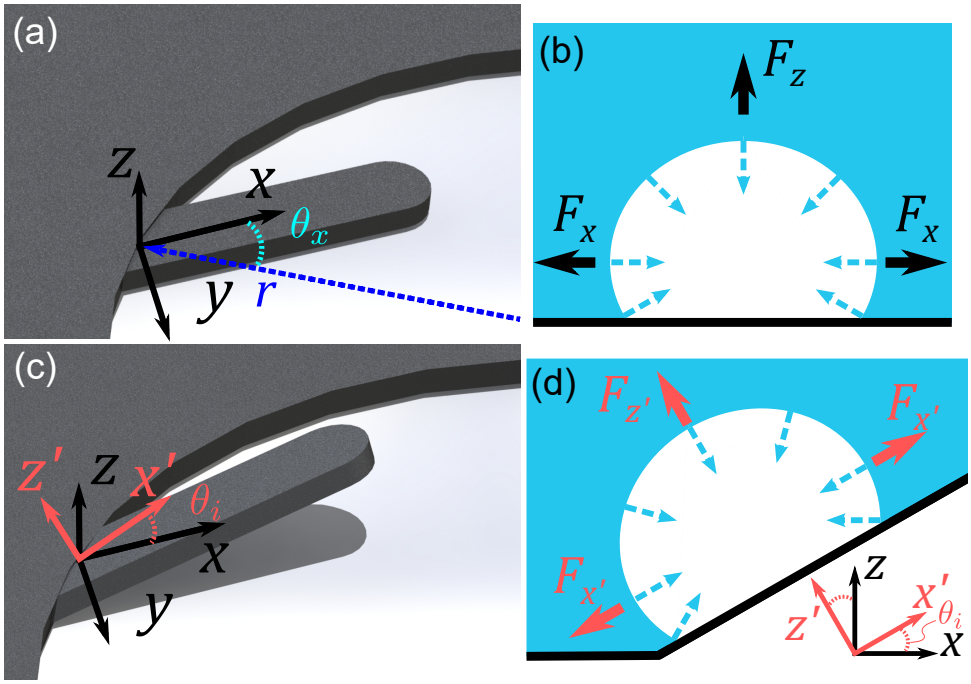

Figure 5: (a) Rendered image of an indent after planar fabrication where the x-axis (along the indent) is at an angle of θ_x with the r-axis; (b) Depiction of the evaporative momentum force on the planar indent; (c) 3D render image of the indent rotated about the y-axis by an angle θ_i; (d) Depiction of the evaporative momentum force on the rotated indent indicating a net evaporative momentum force along the z' axis. This net force has a component perpendicular to r-axis ($\propto \sin(\theta_i)\sin(\theta_x)$), , which drives the rotation of the liquid and the solid rotor. The blue dashed arrows indicate the movement of vapor from the interface into the bubble that produces an outward evaporative momentum force on the interface.

Here, q''_I is the heat flux across the liquid vapor interface, ρ_v is the vapor density, h_{lv} is the latent heat of vaporization and A_{sf} is the surface area of the bubble ($A_{sf} \propto D^2$, where D is the bubble diameter). For a flat surface, a net evaporative momentum force in the z-direction (F_z in Figure 5 (b)) detaches the bubble from the surface (coupled with buoyancy forces). On our inclined indents (Figure 5 (c)), the bubble, or the surrounding liquid, experiences a net force in the z' direction ($F_{z'}$ in Figure 5 (d)), which propels the liquid volume in a direction opposite to the orientation of the protrusions. This net force has a component perpendicular to r-axis ($\propto \sin(\theta_i)\sin(\theta_x)$).

4.1 Analytical model

The angular acceleration of the rotor can be expressed as the difference of the driving torque from bubble nucleation $\Gamma_b (\propto RF_M$, R is the droplet radius, assumed equal to the radial position of the indents) and the resistance to the rotor rotation. The main sources of resistance to the rotation of the solid rotor are friction due to contact line dynamics at the bubble nucleation sites, viscous losses in the droplet and aerodynamic drag from the surrounding air. Due to the significantly small contact area of the liquid with the bubble nucleation sites, we have assumed that the contact line dynamics do not provide a significant resistance to the flow. The resisting torque due to aerodynamic drag on the rotor can be written as $\Gamma_a \sim \rho_a \omega^2 R^5 / Re_{rot}$, where $Re_{rot} = \rho_a R^2 \omega / \mu_a$, R is the radius of the solid rotor, ρ_a and μ_a are the density and viscosity of the air, respectively [48]. For the experimental conditions, Γ_a scales as approximately 10^{-10} Nm. Therefore, only viscous drag due to the droplet on the solid rotor is considered as the dominant

resistance to flow, which scales linearly with the rotation velocity. Assuming the torque from the bubble nucleation as a pulsed input, a simplistic lumped equation of motion of the solid rotor and liquid rotation can be written as (assuming same angular speed of the solid rotor and the liquid):

$$(I_p + I_l)\dot{\omega}_p + c_v\omega = \Gamma_b f(t), \tag{2}$$

where, ω is the instantaneous angular speed of the rotor, I_p and I_l is the moment of inertia of the solid rotor and water, respectively, c_v is the coefficient of viscous damping, Γ_b is the amplitude of the torque produced by the bubble nucleation and $f(t)$ is the pulsed torque input function:

$$f(t) = \frac{\tau}{t_p} + \sum_{n=1}^{\infty} \frac{2}{n\pi} \sin\left(\frac{\pi n\tau}{t_p}\right) \cos\left[\frac{2\pi n}{t_p}(t - \tau/2)\right]. \tag{3}$$

Here, τ is the pulse width and t_p is the time-period of the pulse. We solve equation 2 using superposition ($\omega = \omega_1 + \omega_2$) by solving the following equations:

$$\dot{\omega}_1 + c_I\omega_1 = c_G\frac{\tau}{t_p}, \tag{4}$$

and,

$$\dot{\omega}_2 + c_I\omega_2 = c_G \sum_{n=1}^{\infty} g(n) \cos\left(\frac{2\pi n}{t_p}t\right), \tag{5}$$

where, $c_I = c_v/(I_p + I_l)$, $c_G = \Gamma_b/(I_p + I_l)$ and,

$$g(n) = \frac{2}{n\pi} \sin\left(\frac{\pi n\tau}{t_p}\right). \tag{6}$$

Solving equation 4 and equation 5, and using the initial conditions, $\omega = 0$ at $t = 0$, the speed of the rotor is obtained as:

$$\omega = \frac{\Gamma_b\tau}{c_v t_p}(1 - e^{-c_I t}) + c_G \sum_{n=1}^{\infty} \frac{g(n)}{r} \left[\cos\left(\frac{2\pi n}{t_p}t - k\right) - \cos\left(\frac{\pi n\tau}{t_p} + k\right) e^{-c_I t}\right]. \tag{7}$$

Here, $r = \sqrt{c_I^2 + (2\pi n/t_p)^2}$ and $k = \tan^{-1}[2\pi n/(c_I t_p)]$. From equation 7 the terminal speed can be approximated as $\omega_t = \Gamma_b\tau/(c_v t_p)$ and the starting torque on the disk as $\Gamma_0 = I_p\Gamma_b\tau/t_p(I_p+I_l)$. Both these values depend on the pulse width via the ratio τ/t_p. In the transition boiling engine this ratio τ/t_p corresponds to the ratio of bubble growth time (t_g) and the sum of bubble growth time, departure time (t_d) and wait time for liquid re-wetting (t_w), i.e. cycle time, which varies between 0.2-0.25 [49, 50]. However, in the Leidenfrost state the concept of cycle time does not exist as there is a continuous production of vapor between the liquid and the hot surface. As there is no liquid re-wetting and instantaneous bubble (vapor) production and departure, we can consider the cycle time is equal to the bubble growth time, i.e., $\tau/t_p = 1$. By inserting $\tau/t_p = 1$ in equation 7, the dynamics of the Leidenfrost engine are obtained, as the rotation is powered continuously by the viscous drag from the rectified vapor [14, 15]. It is important to note here that in the reported mm-scale Leidenfrost engines the presence of grooves provide an inertial resistance ($\omega = \omega_t \tanh(ct)$), as opposed to the almost featureless viscous resistance from the substrate in the transition boiling engine ($\omega = \omega_t(1 - e^{-ct})$); c is a constant.

Although the bubble frequency increases at higher superheats [51], the ratio τ/t_p remains mostly invariant in the transition boiling regime [49, 50, 52], while to the best of our knowledge, no such data exists in the transition boiling regime. Therefore, to explain the observations in Figure 4, we look at the variation of Γ_b with the wall superheat ($T_w - T_{sat}$), where T_{sat} is the saturation temperature of the liquid. Typical bubble sizes generated in our experiment

are of the order of the indent size, i.e., D =300 µm in diameter (Supplementary information, Figure S1). Due to a limited visual access to the nucleation site, it is difficult to determine the dependence of bubble nucleation on wall superheat. Therefore, we use analytical expressions, such as that proposed by Zhao *et al* [53]:

$$D = \frac{4k_l(T_w - T_{sat})}{\rho_v h_{lv}\sqrt{0.64Pr\ \alpha_l}}\sqrt{t}, \tag{8}$$

where, k_l is the thermal conductivity of the liquid, ρ_v is the density of vapor, Pr is the Prandtl number, α_l is the thermal diffusivity of the liquid and t is time. Equation 8 is derived using a microlayer heat transfer model. In this model a hemispherical growing bubble is assumed to trap a thin microlayer of liquid between the bubble and the surface. The thickness of this microlayer is expressed by $\delta_0 = \sqrt{0.64Pr\ \alpha_l t}$ [54]. The bubble grows due to the evaporation of this thin microlayer. It is assumed that the latent heat of evaporation of the microlayer is balanced by the heat conduction from the wall through the microlayer. Another model for determining bubble growth characteristics is the contact line heat transfer model, which assumes that evaporative heat transfer at the contact line is the main source of heat transfer/bubble growth [55–57]. It is important to note that these models also provide a similar relationship of $D \propto (T_w - T_{sat})$.

Previous experiments in the transition boiling regime have shown that $q''_I \propto (T_w - T_{sat})^{-1.28}$ [45]. Therefore, the variation of the boiling torque Γ_b with wall superheat is obtained as $\Gamma_b \propto (T_w - T_{sat})^{-0.56}$. The terminal angular speed, $\omega_t = \Gamma_b\tau/(c_v t_p)$, also follows a similar variation with temperature. Figure 4 demonstrates an agreement of these trends with the experimental data for the two deposited drop volumes. However, the predictions disagree with the torque data for V_d=50 µL. These might be due to variation in the time delay between when the water is deposited on the substrate and when the solid rotor is lowered on the water volume. During this time, the water volume (which determines the the rotation) changes depending on the temperature. At such low volumes, these volume changes can affect the torques obtained significantly. With an increase in the deposited volume the liquid inertia (I_l) and viscous damping coefficient c_v increase, which decreases the terminal speed and starting torque, as observed with the data for V_d =100 µL in Figure 4. As explained earlier, for V_d=140 µL, the higher torque and angular speed obtained is likely due to additional nucleation sites created due to the water volume interacting with the side walls.

4.2 Propulsion efficiency

To calculate and compare the efficiencies of the transition and Leidenfrost engines, a microheater is used as a heat source in a thermally insulated experimental rig (shown in Supplementary Figure S2). A micro-grooved turbine-like substrate is used (with channels of width W = 100 µm and depth D = 90 µm) to calculate efficiency of a Leidenfrost engine at a similar device scale [15] (Supplementary Figure S2). The torque in a Leidenfrost engine scales significantly with the system size: $\Gamma_p \propto R^3W/D^3$, where R is the radius of the rotor, W is the width of the channels and D is the depth of the channels, where, for (R, W, D) = (15 mm, 1 mm, 100 µm), the torque on the rotor is of the order of 1×10^{-7} N m [15]. Using these scalings for the present system size i.e. (R, W, D) = (3 mm, 100 µm, 90 µm) the torque is of the order of 1×10^{-10} N m, which is comparable to the torque obtained experimentally at 280 °C: 3.94×10^{-10} N m.

The transition boiling engine consumes a power of 20 W for a substrate temperature of 280 °C and provides an efficiency of 3.3×10^{-5} % (Output power: 1.56×10^{-5} W). The output power obtained here is equal to lighting approximately 125 LEDs, considering one LED consumes almost 0.12 µW. Whereas, the Leidenfrost engine, consumes a power of 12 W at the same temperature giving an efficiency of 4.7×10^{-8} % (Output power: 5.64×10^{-9} W). Compared to the typical torques obtained from the transition boiling engine (Figure 4 (b)), the Leidenfrost engine provides a much lower torque and power output.

Assuming that the energy spent in replenishing the evaporating liquid is neglected, the efficiency of the transition boiling engine is calculated by $\eta = nP_o/\dot{Q}_{in}$, where $P_o = \Gamma_b\omega_t/\sqrt{3}$ is the output power, n is the number of indents or bubble nucleation site and $\dot{Q}_{in}$ is the input heat energy. Considering that bubble generation is highly localised to just the indents, we assume that a significant heat energy input is spend in levitating the liquid, therefore, $\dot{Q}_{in} = \rho_v h_{lv} v_0 \pi R^2$, where $v_0 = k_v(T_w - T_{sat})/(\rho_v h_{lv} h)$, k_v is the thermal conductivity of the vapor and h is the Leidenfrost vapor layer thickness [16]. As $\omega_t = \Gamma_b\tau/(c_v t_p)$, $P_o \propto \Gamma_b^2/c_v$, where $c_v = 2\pi\mu_l R^4/4H$, where μ_l is the viscosity of the liquid and H is the height of the liquid droplet; the derivation of c_v assumes a Couette flow in the liquid volume [15]. Cnsidering $n \propto R$. we find that the power output does not depend on the device scale R, which implies that $\eta \propto 1/R^2$, i.e., the efficiency of the engine should increase with reduced system scales.

In the transition boiling engine a significant amount of heat is spent in providing lubrication via the Leidenfrost effect. However, superhydrophobic coatings on the base and the confining walls can be used to provide sufficient lubrication without the need of a Leidenfrost state [28]. This coating based lubrication significantly reduces the energy requirement for inducing propulsion and can be used to waste heat energy recovery or remote sensing applications [41], where the rotation can be converted to electrical energy using magnetic nanoparticles suspended in the liquid or magnets coupled to the rotor [14]. Through a coating based lubrication, propulsion can also be driven by bubbles generated through localised heating either using lasers [58, 59] or patterned electrodes [24] for mixing biological fluids in lab-on-a-chip devices for healthcare diagnostics [40].

5 Conclusion

In this work we demonstrate a new type of micro-engine utilising two types of boiling mechanisms: controlled local bubble nucleation due to transition boiling is used to propel a solid coupled to a liquid rotor via surface tension, while the Leidenfrost effect is used as an almost frictionless vapor bearing. The propulsion mechanism is attributed to the evaporative momentum force produced on the liquid-vapor interface of the nucleating bubbles. The terminal rotation speed decreases with increasing temperature, which is attributed to the decrease in heat flux with increasing wall superheat. The transition boiling engine shows an efficiency enhancement of almost three orders of magnitude compared to a Leidenfrost engine which uses vapor entrainment as a propulsion mechanism. By focusing on further integration of the engine for continuous operation and electricity generation and employing surface wettability modifications to lower operating temperatures, our work offers potential for autonomous remote sensing based on waste energy harvesting. The concept of boiling induced controlled bubble-based propulsion offers potential for mixing application in lab-on-a-chip systems and coolants in microgravity via controlled heating through lasers or selective electrode patterning.

6 Acknowledgements

The authors would like to thank funding from Royal Society RGS\R1\221020 and EPSRC grants EP/P005896/1, EP/P005705/1 and EP/P005896/2.

References

[1] Ravi Kishore and Shashank Priya. A review on low-grade thermal energy harvesting: materials, methods and devices. *Materials*, 11(8):1433, 2018.

[2] Christopher Depcik. Exploring the Potential of Combustion on Titan. *SAE International Journal of Aerospace*, 11(1):27–45, 2018.

[3] C H Lee, K C Jiang, P Jin, and P D Prewett. Design and fabrication of a micro Wankel engine using MEMS technology. *Microelectronic Engineering*, 73-74(1):529–534, 6 2004.

[4] Changgu Lee, Mokhtar Liamini, and Luc G. Frechette. A silicon microturbopump for a rankine-cycle power-generation microsystempart II: Fabrication and characterization. *Journal of Microelectromechanical Systems*, 20(1):326–328, 2011.

[5] Samuel L. Miller, Glen LaVigne, M. Steven Rodgers, Jeffry J. Sniegowski, J. P. Waters, and Paul J. McWhorter. Routes to failure in rotating MEMS devices experiencing sliding friction. *Micromachined Devices and Components III*, 3224(September 1997):24, 1997.

[6] I. S Y Ku, T. Reddyhoff, A. S. Holmes, and H. A. Spikes. Wear of silicon surfaces in MEMS. *Wear*, 271(7-8):1050–1058, 2011.

[7] Huizeng Li, Wei Fang, Yanan Li, Qiang Yang, Mingzhu Li, Qunyang Li, Xi Qiao Feng, and Yanlin Song. Spontaneous droplets gyrating via asymmetric self-splitting on heterogeneous surfaces. *Nature Communications*, 10(950), 2019.

[8] Lei Lei Wang, Li Chen, Jing Zhang, Jin Ming Duan, Lei Weng, Zhan Hua Silber-Li, Xu Zheng, and Hai Hang Cui. Efficient Propulsion and Hovering of Bubble-Driven Hollow Micromotors underneath an Air-Liquid Interface. *Langmuir*, 34(35):10426–10433, 2018.

[9] Junwoo Suh, Debra Cytrynowicz, Frank M. Gerner, and H. Thurman Henderson. A MEMS bubble pump for an electronic cooling device. *Journal of Micromechanics and Microengineering*, 20(12), 2010.

[10] B Sun, F Han, L Li, and Q Wu. Rotation Control and Characterization of High-Speed Variable-Capacitance Micromotor Supported on Electrostatic Bearing. *IEEE Transactions on Industrial Electronics*, 63(7):4336–4345, 2016.

[11] B Assadsangabi, M H Tee, and K Takahata. Electromagnetic Microactuator Realized by Ferrofluid-Assisted Levitation Mechanism. *Journal of Microelectromechanical Systems*, 23(5):1112–1120, 2014.

[12] Luc G. Fréchette, Stuart A. Jacobson, Kenneth S. Breuer, Fredric F. Ehrich, Reza Ghodssi, Ravi Khanna, Chee Wei Wong, Xin Zhang, Martin A. Schmidt, and Alan H. Epstein. High-speed microfabricated silicon turbomachinery and fluid film bearings. *Journal of Microelectromechanical Systems*, 14(1):141–152, 2005.

[13] Mei Lin Chan, Brian Yoxall, Hyunkyu Park, Zhaoyi Kang, Igor Izyumin, Jeffrey Chou, Mischa M. Megens, Ming C. Wu, Bernhard E. Boser, and David A. Horsley. Design and characterization of MEMS micromotor supported on low friction liquid bearing. *Sensors and Actuators, A: Physical*, 177:1–9, 2012.

[14] Gary G Wells, Rodrigo Ledesma-Aguilar, Glen McHale, and Khellil Sefiane. A sublimation heat engine. *Nature Communications*, 6(6390), 2015.

[15] Prashant Agrawal, Gary G Wells, Rodrigo Ledesma-Aguilar, Glen McHale, Anthony Buchoux, Adam Stokes, and Khellil Sefiane. Leidenfrost heat engine: Sustained rotation of levitating rotors on turbine-inspired substrates. *Applied Energy*, 240:399–408, 2019.

[16] Prashant Agrawal, Gary G. Wells, Rodrigo Ledesma-Aguilar, Glen McHale, and Khellil Sefiane. Beyond Leidenfrost levitation: A thin-film boiling engine for controlled power generation. *Applied Energy*, 287(January):116556, 2021.

[17] Johann Gottlob Leidenfrost. On the fixation of water in diverse fire. *International Journal of Heat and Mass Transfer*, 9(11):1153–1166, 1966.

[18] Guillaume Lagubeau, Marie Le Merrer, Christophe Clanet, and David Quéré. Leidenfrost on a ratchet. *Nature Physics*, 7(5):395–398, 2011.

[19] Dan Soto, Guillaume Lagubeau, Christophe Clanet, and D Quere. Surfing on a herringbone. *Physical Review Fluids*, 1(013902), 2016.

[20] Tobias Baier, Guillaume Dupeux, Stefan Herbert, Steffen Hardt, and David Quéré. Propulsion mechanisms for Leidenfrost solids on ratchets. *Physical Review E - Statistical, Nonlinear, and Soft Matter Physics*, 87(021001 (R)), 2013.

[21] L E Dodd, P Agrawal, M T Parnell, N R Geraldi, B B Xu, G G Wells, S Stuart-Cole, M I Newton, G McHale, and D Wood. Low-Friction Self-Centering Droplet Propulsion and Transport Using a Leidenfrost Herringbone-Ratchet Structure. *Physical Review Applied*, 2019.

[22] James M Arter, David J Cleaver, Kei Takashina, and Andrew T Rhead. Self-propelling Leidenfrost droplets on a variable topography surface. *Applied Physics Letters*, 113(243704), 2018.

[23] Rebecca L. Agapov, Jonathan B. Boreyko, Dayrl P. Briggs, Bernadeta R. Srijanto, Scott T. Retterer, C. Patrick Collier, and Nickolay V. Lavrik. Asymmetric wettability of nanostructures directs Leidenfrost droplets. *ACS Nano*, 8(1):860–867, 1 2014.

[24] Linzi E Dodd, Prashant Agrawal, Matthew T. Parnell, Nicasio R. Geraldi, Ben B Xu, Gary G Wells, Simone Stuart-Cole, Michael I Newton, Glen McHale, and David Wood. Low-Friction Self-Centering Droplet Propulsion and Transport Using a Leidenfrost Herringbone-Ratchet Structure. *Physical Review Applied*, 11(034063), 3 2019.

[25] Ambre Bouillant, Timothée Mouterde, Philippe Bourrianne, Antoine Lagarde, Christophe Clanet, and David Quéré. Leidenfrost wheels. *Nature Physics*, 14:1188–1192, 2018.

[26] Guillaume Dupeux, Tobias Baier, Vincent Bacot, Steffen Hardt, Christophe Clanet, and David Quéré. Self-propelling uneven Leidenfrost solids. *Physics of Fluids*, 25(051704), 2013.

[27] Hao Xu, Antoine Thissandier, Ruijie Zhao, Peng Tao, Chengyi Song, Jianbo Wu, Wen Shang, and Tao Deng. Self-propelled rotation of paper-based Leidenfrost rotor. *Applied Physics Letters*, 114(113703), 2019.

[28] Guillaume Dupeux, Philippe Bourrianne, Quentin Magdelaine, Christophe Clanet, and David Quéré. Propulsion on a superhydrophobic ratchet. *Scientific Reports*, 4(5280), 2014.

[29] Qiang Ma, Xiaomin Wu, Tong Li, and Fuqiang Chu. Droplet boiling on heated surfaces with various wettabilities. *Applied Thermal Engineering*, 167(114703), 2020.

[30] E. Teodori, T. Valente, I. Malavasi, A. S. Moita, M. Marengo, and A. L.N. Moreira. Effect of extreme wetting scenarios on pool boiling conditions. *Applied Thermal Engineering*, 115:1424–1437, 2017.

[31] H. Linke, B. J. Alemán, L. D. Melling, M. J. Taormina, M. J. Francis, C. C. Dow-Hygelund, V. Narayanan, R. P. Taylor, and A. Stout. Self-propelled leidenfrost droplets. *Physical Review Letters*, 96(154502), 2006.

[32] Tong-Miin Liou, Chia-Yen Chan, and Kuan-Cheng Shih. Effects of actuating waveform, ink property, and nozzle size on piezoelectrically driven inkjet droplets. *Microfluidics and Nanofluidics*, 8(5):575–586, 2010.

[33] Ping Hei Chen, Wen Cheng Chen, Pei Pei Ding, and S. H. Chang. Droplet formation of a thermal sideshooter inkjet printhead. *International Journal of Heat and Fluid Flow*, 19(4):382–390, 8 1998.

[34] Tieyan Si, Xian Zou, Zhiguang Wu, Tianlong Li, Xin Wang, Krasnyuk Ivan Ivanovich, and Qiang He. A Bubble-Dragged Catalytic Polymer Microrocket. *Chemistry - An Asian Journal*, 14(14):2460–2464, 2019.

[35] Wei Gao, Sirilak Sattayasamitsathit, Jahir Orozco, and Joseph Wang. Efficient bubble propulsion of polymer-based microengines in real-life environments. *Nanoscale*, 5(19):8909–8914, 2013.

[36] Hong Wang, James Guo Sheng Moo, and Martin Pumera. From Nanomotors to Micromotors: The Influence of the Size of an Autonomous Bubble-Propelled Device upon Its Motion. *ACS Nano*, 10(5):5041–5050, 2016.

[37] Jian Feng, Junqi Yuan, and Sung Kwon Cho. Micropropulsion by an acoustic bubble for navigating microfluidic spaces. *Lab on a Chip*, 15(6):1554–1562, 2015.

[38] Xiaolin Wang, Daniel Attinger, and Francisco Moraga. A Micro-Rotor Driven by an Acoustic Bubble. *Nanoscale and Microscale Thermophysical Engineering*, 10(4):379–385, 12 2006.

[39] Xiantong Yan, Wanghuai Xu, Yajun Deng, Chao Zhang, Huanxi Zheng, Siyan Yang, Yuxin Song, Pengyu Li, Xiaote Xu, Yue Hu, Luwen Zhang, Zhengbao Yang, Steven Wang, and Zuankai Wang. Bubble energy generator. *Science Advances*, 8(25):7698, 2022.

[40] Q. Chi, Z. Wang, F. Tian, J. You, and S. Xu. A Review of Fast Bubble-Driven Micromotors Powered by Biocompatible Fuel: Low-Concentration Fuel, Bioactive Fluid and Enzyme. *Micromachines (Basel)*, 10(9):537, 2018.

[41] S. Sinha-Ray, W. Zhang, B. Stolz, R. P. Sahu, S. Sinha-Ray, and A. L. Yarin. Swing-like pool boiling on nano-textured surfaces for microgravity applications related to cooling of high-power microelectronics. *npj Microgravity*, 3:9, 2017.

[42] Niroh Nagai and Shigefumi Nishio. Leidenfrost temperature on an extremely smooth surface. *Experimental Thermal and Fluid Science*, 12(3):373–379, 1996.

[43] T. Y. Xiong and M. C. Yuen. Evaporation of a liquid droplet on a hot plate. *International Journal of Heat and Mass Transfer*, 34(7):1881–1894, 1991.

[44] Daniel Orejon, Khellil Sefiane, and Yasuyuki Takata. Effect of ambient pressure on Leidenfrost temperature. *Physical Review E - Statistical, Nonlinear, and Soft Matter Physics*, 90(5):1–6, 2014.

[45] J. D. Bernardin and Issam Mudawar. Transition boiling heat transfer of droplet streams and sprays. *Journal of Heat Transfer*, 129(11):1605–1610, 2007.

[46] S. G. Kandlikar. Controlling bubble motion over heated surface through evaporation momentum force to enhance pool boiling heat transfer. *Applied Physics Letters*, 102(5), 2013.

[47] Pruthvik A. Raghupathi and Satish G. Kandlikar. Evaporation momentum force on a bubble under asymmetric temperature conditions. *ASME International Mechanical Engineering Congress and Exposition, Proceedings (IMECE)*, 8B, 2014.

[48] Hermann Schlichting and Klaus Gersten. Boundary-Layer Theory. 2017.

[49] Craig Gerardi, Jacopo Buongiorno, Lin wen Hu, and Thomas McKrell. Study of bubble growth in water pool boiling through synchronized, infrared thermometry and high-speed video. *International Journal of Heat and Mass Transfer*, 53(19-20):4185–4192, 2010.

[50] G. Giustini, Iljin Kim, and Hyungdae Kim. Comparison between modelled and measured heat transfer rates during the departure of a steam bubble from a solid surface. *International Journal of Heat and Mass Transfer*, 148:119092, 2020.

[51] Yinxiao Li, Ke Zhang, Ming Chang Lu, and Chuanhua Duan. Single bubble dynamics on superheated superhydrophobic surfaces. *International Journal of Heat and Mass Transfer*, 99:521–531, 2016.

[52] S J D van Stralen, M S Sohal, R Cole, and W M Sluyter. Bubble growth rates in pure and binary systems: Combined effect of relaxation and evaporation microlayers. *International Journal of Heat and Mass Transfer*, 18(3):453–467, 1975.

[53] Yao Hua Zhao, Takashi Masuoka, and Takaharu Tsuruta. Unified theoretical prediction of fully developed nucleate boiling and critical heat flux based on a dynamic microlayer model. *International Journal of Heat and Mass Transfer*, 45(15):3189–3197, 2002.

[54] M.G. Cooper and A.J.P. Lloyd. The microlayer in nucleate pool boiling. *International Journal of Heat and Mass Transfer*, 12(8):895 – 913, 1969.

[55] M. S. Plesset and S. A. Zwick. The growth of vapor bubbles in superheated liquids. *Journal of Applied Physics*, 25(4):493–500, 1954.

[56] H. K. Forster and N. Zuber. Growth of a vapor bubble in a superheated liquid. *Journal of Applied Physics*, 25(4):474–478, 1954.

[57] L Biasi, P Stipari, and A Tozzi. Bubble growth in non-uniform temperature fields. *Chemical Engineering Science*, 26(6):867–873, 1971.

[58] V.M. Chudnovskii, V.I. Yusupov, A.V. Dydykin, V.I. Nevozhai, A.Yu. Kisilev, S.A. Zhukov, and V.N. Bagratashvili. Laser-induced boiling of biological liquids in medical technologies. *Quantum Electronics*, 47(4):361, may 2017.

[59] Atsushi Takamizawa, Shinji Kajimoto, Jonathan Hobley, Koji Hatanaka, Koji Ohta, and Hiroshi Fukumura. Explosive boiling of water after pulsed ir laser heating. *Phys. Chem. Chem. Phys.*, 5:888–895, 2003.